 CMES, vol.87, no.6, pp.505-528, 2012

MicroCT/Micromechanics-Based Finite Element Models and Quasi-Static Unloading Tests Deliver Consistent Values for Young's Modulus of Rapid-Prototyped Polymer-Ceramic Tissue Engineering Scaffold

K.W. Luczynski[1], A. Dejaco[1], O. Lahayne[1]
J. Jaroszewicz[2], W.Swieszkowski[2] and C. Hellmich[1]

Abstract: A 71 volume-% macroporous tissue engineering scaffold made of poly-l-lactide (PLLA) with 10 mass-% of pseudo-spherical tri-calcium phosphate (TCP) inclusions (exhibiting diameters in the range of several nanometers) was microCT-scanned. The corresponding stack of images was converted into regular Finite Element (FE) models consisting of around 100,000 to 1,000,000 finite elements. Therefore, the attenuation-related, voxel-specific grey values were converted into TCP-contents, and the latter, together with nanoindentation tests,entered a homogenization scheme of the Mori-Tanaka type, as to deliver voxel-specific (and hence, finite element-specific) elastic properties. These FE models were uniaxially loaded, giving access to the macroscopic Young's modulus of the entire scaffold, amounting to E_{FE}=142.86±2.68MPa. The reliability of the FE simulations was shown through comparison with results from quasi-static unloading tests on the same scaffold sample, delivering an experimental value of the longitudinal Young's modulus, $E_{unl} = 125.85 \pm 19.33$MPa. The uniaxial test simulations also provided access to Poisson's ratios in the transverse material directions, which turned out to be quasi-cubic, and amounted, on average, to 0.0638±0.0136.This is much smaller than the Poisson's ratio of the solid phase made up of PLLA-TCP, which amounted to 0.44. This indicates that on the microscopic level, the pores are, on average, much more deformed, than the solid phase made of PLLA-TCP. Namely, significant (micro)deformation of the latter is restricted to the junctions between the rapid-prototyped beams making up the scaffold.

Keywords: MicroCT, Finite Element simulation, Young's modulus, quasi-static

[1] Vienna University of Technology, Institute for Mechanics of Materials and Structures, Vienna, Austria.
[2] Warsaw University of Technology, Faculty for Materials Science and Engineering, Warsaw, Poland.

unloading tests, tissue engineering scaffolds.

1 Introduction

Tissue engineering is a discipline striving for regeneration of such biological tissues which *a priori* do not have any self-healing capability (as is e.g. the case for cartilage or large bone defects); this task is tackled through the combination of growth factors and biological cells, with so-called tissue engineering scaffolds to be implanted in the damaged organism [Langer and Vacanti (1993); Khademhosseini et al. (2005); Park et al. (2007); Mouriño et al. (2012)]. Traditionally, trial-and-error strategies were employed to find out functioning scaffold-factor-cell combinations [Khademhosseini et al. (2005)]. In the course of such studies, it became obvious that tissue engineering scaffolds have not only to be biocompatible, but they also need to ensure sufficient load carrying capacity, and nevertheless they have to enable tissue ingrowth [Rezwan et al. (2006); Wagoner Johnson and Herschler (2011); Janicki and Schmidmaier (2011)]. The latter requirement implies use of porous scaffolds, with pore sizes of one to several hundred micrometers [Rezwan et al. (2006); Woodard et al. (2007)]. With increasing porosity, the mechanical strength of the scaffolds decreases (Fritsch et al. 2009), while bone ingrowth is facilitated [Rezwan et al. (2006); Janicki and Schmidmaier (2011); Woodard et al. (2007)]. Besides the scaffolds' mechanical strength, their elasticity is of importance, since it is the elasticity which predominantly drives the stress distribution in organ-implant systems [Rezwan et al. (2006); Chen et al. (2011)], and this distribution should deviate as little as possible from the natural state (without implant). In this context, the potential benefit of computer-based design tools for tissue engineering solutions has been realized more and more in recent years, and engineering scientists have proposed the application of numerical methods such as the Finite Element (FE) method [Zienkiewicz and Taylor (2005)] and of semi-analytical tools such as homogenization theory and continuum micromechanics [Eshelby (1957); Benveniste (1987); Zaoui (2002); Dormieux et al. (2006)] for the simulation of the mechanical behavior of tissue engineering scaffolds, or of compounds built up of both scaffolds and tissue engineered, e.g. biological cell-produced, new bone tissue [Lacroix et al. (2006); Sandino et al. (2008); Bertrand and Hellmich (2009); Fritsch et al. (2009); Scheiner et al. (2009); Dejaco et al. (2012)]. While it is generally accepted that geometrical and microstructural details of such scaffolds can be straightforwardly extracted from micro Computer Tomographic (microCT) images, and transferred to fine Finite Element meshes [Lacroix et al. (2006)], the assignment of material properties on an element-per-element basis turns out as a much more tricky issue. As a respective remedy for ceramic-based biomaterials [Komlev et al. (2010)], we have recently proposed [Scheiner et al. (2009);

Dejaco et al. (2012)] to translate the X-ray attenuation-related grey values making up a microCT image, into voxel-specific (nano)porosities, and to resolve the microstructure (or nanostructure) *within* each finite element in terms of a continuum micromechanics representation [Fritsch et al. (2009)] linking (nano) porosity to material properties, as to arrive at tissue property maps across the entire imaged scaffold. These property maps turned out as reasonable input for FE simulations [Scheiner et al. (2009); Dejaco et al. (2012)]. In the present paper, we extend this strategy to rapid-prototyped polymer-ceramic scaffolds [Swieszkowski et al. (2007)]. Therefore, we undertake the following steps: We report microCT scanning and porosity determination of a scaffold made of poly-l-lactide (PLLA) reinforced by nanometer-sized particles of tri-calcium phosphate (TCP), see Section 2.1. Thereafter, we report on a nanoindentation campaign giving access to the micrometer-scale elastic properties of the aforementioned material, see Section 2.2. These experimental data enter a Finite Element study based on voxel-specific elastic properties derived from X-ray physics [Crawley et al.(1988); Hellmich et al. (2008); Scheiner et al. (2009)] and micromechanics, see Section 3.1, where we are interested in uniaxial compression as a typical loading scenario, see Section 3.2. As a rule [Popper (1934)], simulation results, as any other theoretical propositions, need independent experimental validation, and therefore, in Section 4, we report on quasi-static unloading tests performed on the very scaffold which was simulated before. The key results of FE simulations are documented and discussed thereafter, in Section 5.

2 Experiments for model development

2.1 MicroCT imaging for geometry and porosity assessment

A tissue engineering scaffold [see Fig. 1(a)] with dimensions of 12.05mm $\times$ 6.15mm $\times$ 6.10mm, and mass density of 0.42g/cm^3 was produced by rapid-prototyping via fused deposition modeling, as described in [Swieszkowski et al. (2007)]. The solid material consisted of a poly-l-lactide (PLLA) matrix and pseudo-spherical tri-calcium phosphate inclusions (TCP powder p08004c, Progentix, Bilthoven, The Netherlands; with particle diameters in the range of several nanometers). These TCP nanocrystals, which partially cluster, at mutually distant spots, into larger agglomerations appearing as light spots in Fig. 1(b), make up 10% of the total mass. A region of interest (ROI), comprising the first 5.46 mm of the 12.05 mm height of the tested scaffold sample, was scanned in a SKYSCAN 1172 desktop microCT machine. Respective projection images were Radon-transformed, by means of the SKYSCAN's NRecon v1.6.1.2 software, to a stack of 8bit grey-scaled 2D images with a pixel size of 9.92 microns, which led to 3D image volume of $760\times760\times550$

voxels.

It is instructive to plot a histogram of all X-ray attenuation-related grey values making up the 3D image domain (see Fig. 2). The histogram shows two peaks, with corresponding grey values belonging to the gaseous domain and the solid domain of the scaffold, respectively. We use the minimum between the "air peak" and the "solid peak" as the threshold GV_{thr}=*65 to distinguish between the solid voxels (with* $GV > GV_{thr}$*) and the air voxels (with* $GV \leq GV_{thr}$*)*.The macroporosity was quantified as the ratio of the number of voxels occupied by pores to the total number of voxels within the chosen ROI, using the image treatment software CTAn v1.12 (SKYSCAN, Belgium): it amounted to Φ=71%.

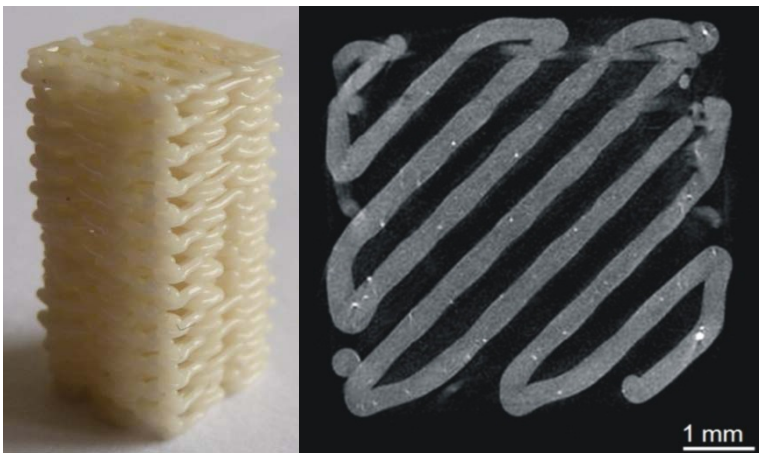

a) b)

Figure 1: PLLA-TCP tissue engineering scaffold with 71% macroporosity: (a) photograph,(b) micro-CT slice of the scaffold's transversal cross-section, with partially visible TCP inclusions (white spots marking high local TCP concentration)

2.2 Micromechanics of solid portion of scaffold: nanoindentation

Nanoindentation has become a standard technique for biomaterial characterization [Khanna et al. (2009)]. Herein, we followed the subsequent protocol: A specimen of the same origin and solid phase composition as the one scanned according to the protocol given in Section 2.1, was embedded in resin (Epofix, Struers, Denmark), and then it was polished with increasingly fine sandpaper (1PM51, Logitech, United Kingdom), until a satisfactorily scratch-free surface of the PLLA-TCP solid was achieved. Thereafter, this surface was indented by means of a Berkovich indenter (TI 900 Triboindenter, Hysitron, Minneapolis, USA). The loading-unloading

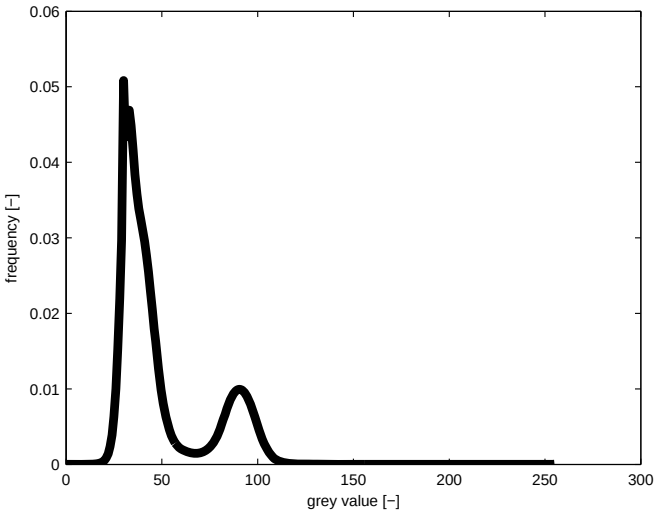

Figure 2: Probability density function of X-ray attenuation-related grey values (GV) throughout the entire 3D microCTimageof the macroporous PLLA-TCP scaffold: all GV values higher than GV_{thr}=65 correspond to solid-filled voxels

rate was set to 300μN/s. A trapezoidal loading mode with 30s holding time, and two different maximum loads of 3mN and 6mN were chosen. This choice resulted in contact areas ranging from 12.04$\pm$0.52μm^2 to *23.53$\pm$0.80μm^2*. When comparing these sizes to the nanometric size of TCP particles dispersed in the PLLA matrix, it becomes obvious that the indentation tests were carried out on the PLLA-TCP composite. For each load, approximately 40 measurements were performed. Load-displacement data were evaluated according to the method of Oliver and Pharr [Oliver and Pharr (2004)], whereby Poisson's ratio of the scaffold's solid portion was assumed to be equal to the one of PLLA, i.e., equal to ν_{PLLA}=0.45 [Balac et al. (2002)]. For the TCP volume fraction prevailing in the present paper, this assumption was validated by a micromechanical approach based on the Mori-Tanaka estimate [Mori and Tanaka (1973)]: Accordingly, the PLLA-TCP composite exhibits a Poisson's ratio which is only 2% (or even less than that) smaller than the one of pure PLLA [Luczynski et al. (2012)]. When averaged over all conducted nanoindentation tests, the Young's modulus of the solid PLLA-TCP portion amounted to E^{indent}=4.52$\pm$0.16GPa.

3 Finite Element model development

3.1 Voxel- and finite element-specific elastic properties, based on X-ray physics and micromechanics

The elastic properties of the solid matrix were derived from X-ray attenuation coefficients as follows: Each voxel occupied by the solid contains a composite material consisting of PLLA matrix (filling volume fraction f_{PLLA}) with TCP inclusions (filling volume fraction f_{TCP}). Hence, the volume fractions fulfill

$$f_{PLLA} + f_{TCP} = 1 \tag{1}$$

For this PLLA-TCP composite, the averagerule for X-ray attenuation coefficients μ reads as [Crawley et al. (1988); Hellmich et al. (2008); Scheiner et al. (2009)]

$$\mu = \mu_{PLLA} f_{PLLA} + \mu_{TCP} f_{TCP} \tag{2}$$

where μ_{PLLA} and μ_{TCP} are the X-ray attenuation coefficients of PLLA and of TCP, respectively. Since the X-ray attenuation coefficients are linearly related to the grey values GV shown in microCT images, it follows from Eq. (2) that

$$GV = GV_{PLLA} f_{PLLA} + GV_{TCP} f_{TCP} \tag{3}$$

with GV_{PLLA}=66 and GV_{TCP} as the grey values of a voxel which is entirely filled by PLLA or by TCP material, respectively. The densest voxel in the images characterized by GV=255, is not entirely filled with TCP, so that we need to identify a TCP-related grey value larger than 255. For the respective "calibration process", we rely on mass and volume measurements, together with mass density averaging, adapting the strategy proposed by [Dejaco et al. (2012)]: at the voxel level, the mass density ρ_{vox} reads as

$$\rho_{vox}(x) = f_{TCP}(x)\rho_{TCP} + [1 - f_{TCP}(x)]\rho_{PLLA} \tag{4}$$

with ρ_{PLLA}=1.25g/cm^3 as the mass density of PLLA, and ρ_{TCP}=3.14g/cm^3 as the mass density of TCP [Blazewicz and Stoch (2004)]. The average, over the entire scaffold, of these voxel-specific mass densities equals to the overall "apparent" mass density of the scaffold sample, ρ_{app}=0.42g/cm^3 (identified as the scaffold's mass over its "apparent" volume; whereby the latter, in case of a cuboid sample, was computed from its dimensions as V_{app}=12.05mm$\times$6.15mm$\times$6.10mm)

$$(1-\Phi)\frac{1}{V}\int_V \rho_{vox}(x)dV = \rho_{app} \tag{5}$$

with Φ as the scaffold's macroporosity (see Section 2.1), V scaffold's solid phase volume, and x representing each voxel occupied by the solid.

Finally, Eq. (1), (3), (4) and (5) allow for numerical determination of GV_{TCP}, resulting in GV_{TCP}=293.5. Then, Eq. (3) can be used to convert voxel-specific grey values into voxel-specific volume fractions of TCP,

$$f_{TCP} = (GV - GV_{PLLA})/(GV_{TCP} - GV_{PLLA}) \tag{6}$$

resulting in volume fractions of TCP ranging from 0 to 0.83 for grey values from 66 to 255, respectively.

Next, this volume fraction enters a micromechanical description of the material found within the individual voxels. Consequently, we regard each and every voxel as a representative volume element (RVE) in the sense of continuum micromechanics (Zaoui, 2002; Dormieux et al, 2006), which has to fulfill the so-called separation of scales requirement: (i) the RVE size (being equal to the voxel size) needs to be small as compared to the characteristic length of the overall structure and/or loading (this will be checked through the convergence study documented in Fig. 5); and (ii) the characteristic length of the RVE needs to be larger than the characteristic size of the inhomogenities within the RVE – in other words, the voxel size needs to be significantly larger than the size of the TCP particles dispersed in the PLLA matrix. Comparing the 9.92 microns edge length of the employed voxels to the nanometer size of the TCP particles entails the second scale separation requirement as fulfilled. Given, in addition, the matrix-inclusion-type morphology of the microstructure found within the individual voxels, we employ the Mori-Tanaka scheme [Eshelby (1957); Mori and Tanaka (1973); Benveniste (1987)] for determination of the voxel-specific fourth-order (homogenized) stiffness tensor $\mathbf{C}^{hom}$ of the PLLA-TCP composite,

$$\mathbf{C}^{\text{hom}} = \left\{(1-f_{TCP})\,\mathbf{c}_{PLLA} + f_{TCP}\mathbf{c}_{TCP} : \left[\mathbf{I} + \mathbf{P}_{PLLA,sph} : (\mathbf{c}_{TCP} - \mathbf{c}_{PLLA})\right]^{-1}\right\} : \left\{(1-f_{TCP})\,\mathbf{I} + f_{TCP}\left[\mathbf{I} + \mathbf{P}_{PLLA,sph} : (\mathbf{c}_{TCP} - \mathbf{c}_{PLLA})\right]^{-1}\right\}^{-1} \tag{7}$$

with

$$\mathbf{C}_{PLLA} = 3k_{PLLA}\mathbf{I}_{vol} + 2G_{PLLA}\mathbf{I}_{dev} \tag{8}$$

and

$$\mathbf{C}_{TCP} = 3k_{TCP}\mathbf{I}_{vol} + 2G_{TCP}\mathbf{I}_{dev} \tag{9}$$

as the isotropic phase stiffnesses of the matrix and the inclusions, respectively. In Eq. (8) and (9) $\mathbf{I}_{vol}$, with components $I_{vol,ijkl}$=1/3$\delta_{ij}\delta_{kl}$ is the volumetric part of the fourth-order unity tensor $\mathbf{I}$, with components I_{ijkl}=1/2($\delta_{ik}\delta_{jl}$+$\delta_{il}\delta_{jk}$); and $\mathbf{I}_{dev} = \mathbf{I} - \mathbf{I}_{vol}$ is the deviatoric part of $\mathbf{I}$. The Kronecker delta δ_{ij} is defined as δ_{ij} =0 for $i \neq j$ and δ_{ij}=1 for $i = j$. Moreover, in Eq. (7), $\mathbf{P}_{PLLA,sph}$ denotes the fourth-order Hill tensor accounting for the spherical shape of the TCP inclusions embedded in the PLLA-matrix. Given the strong chemical similarity of TCP and hydroxyapatite [Dorozhkin (2009)], the elastic properties of the latter were considered: Ultrasound experiments of [Katz and Ukraincik (1971)] on hydroxyapatite deliver the bulk and shear moduliof TCP as k_{TCP}=82.60GPa and G_{TCP}=44.90GPa, respectively. The elastic properties of PLLA, expressed in terms of bulk modulus

$$k_{PLLA} = E_{PLLA}/(3(1-2\nu_{PLLA})) \tag{10}$$

and of shear modulus

$$G_{PLLA} = E_{PLLA}/(2(1+\nu_{PLLA})) \tag{11}$$

followed from the nanoindentation tests of Section 2.2, and from the literature. Namely, Poisson's ratio of PLLA was taken from [Balac et al. (2002)], amounting to ν_{PLLA} = 0.45. Concerning Young's modulus of PLLA (E_{PLLA}), the nanoindentation measurementsof Section 2.2 gave access to the mean value of the Young's modulus of PLLA-TCP composite material, E^{indent}. The latter needs to be equal to the average, over all voxels making up the solid portion of the scaffold in the microCT image, of the attenuation- and micromechanics-based Young's moduli E^{hom} [whereby E^{hom} is the inverse of the first component of the homogenized compliance tensor being itself the inverse of the stiffness tensor of Eq. (7)]. In mathematical terms, this reads as

$$E^{indent} = \frac{1}{V}\int_V E^{\hom}(E_{PLLA}, \nu_{PLLA}, k_{TCP}, G_{TCP}, GV)dV \tag{12}$$

where the functional relationship for E^{hom} follows from Eq. (6) - (11). Eq. (12) allows for the determination of the Young's modulus of PLLA, and the numerically obtained value, E_{PLLA}=3.59GPa, is in a perfect agreement with corresponding value of 3.60GPa found in [Blazewicz and Stoch (2004)].

Finally, use of the aforementioned elastic properties of PLLA and TCP in Eq. (7), while considering Eq. (6), gives access to grey value-specific Young's moduli $E^{hom}(GV)$ and Poisson's ratios $\nu^{hom}(GV)$ throughout the scaffold's solid phase; more precisely, the latter are, in a standard fashion, computed from the compliance tensor

$\mathbf{D}^{hom}=(\mathbf{C}^{hom})^{-1}$, according to:

$$E^{hom}(GV) = 1/D^{hom}_{1111}(GV) \tag{13}$$

$$\nu^{hom}(GV) = -E^{hom}(GV)/D^{hom}_{1122}(GV) \tag{14}$$

In addition to these heterogeneous (grey value-specific) elastic properties throughout the solid portion of the scaffold, also "smeared" homogeneous elastic properties (see Tab. 1) were considered. Remembering that averaging over elastic properties does not *per se* have a theoretical basis [Zaoui (2002)], while the evaluation of volume fractions within reasonably chosen RVEs is one of the fundamentals of micromechanics, we average over all volume fraction-related grey values [see Eq. (6)] in the solid compartment of the microCT image, as to arrive at an averaged grey value GV_{avg} according to

$$GV_{avg} = \frac{1}{N_{sol}} \sum_{GV=66}^{GV=255} (N_{GV} \times GV) = 90 \tag{15}$$

where N_{sol} is the total number of voxels in the solid portion of the scaffold, and N_{GV} is the number of voxels with grey value GV. Specification of Eq. (13) and (14) for GV=GV_{avg} yields the "average" homogeneous elastic properties in terms of Young's modulus and Poisson's ratio as E_{GVavg}=4.51GPa and ν_{GVavg}=0.44, respectively (see also Tab. 1).

Table 1: Elastic properties related to solid compartment of scaffold: poly-l-lactide (PLLA) from nanoindentation and micromechanics (Sections 2.2 and 3.1), tricalcium phosphate (TCP) from ultrasonic experiments (Section 3.1), "average" PLLA-TCP nanocomposite from micromechanics (Section 3.1)

	Young's modulus [GPa]	Poisson's ratio [-]
PLLA	3.59	0.45
TCP	114.04	0.27
PLLA-TCP	4.52	0.44

Finally, regular FE models of the PLLA-TCP-based scaffold were generated from the stack of microCT images analogously to the procedure described in [Dejaco et al. (2012)]. Thereby, 8×8×8, 7×7×7, 6×6×6, 5×5×5, and 4×4×4 voxels were combined into one finite element each, which resulted in Finite Element models with 1.1×10^5, 1.7×10^5, 2.7×10^5, 4.8×10^5, and 9.6×10^5 elements. Thereby, the grey values GV were *either* averaged over the 64 to 512 voxels merged into one finite element each, and converted, according to Eq. (6) - (11) and (13) - (14) into

finite element-specific stiffness properties; *or* all solid finite elements were assigned one pair of Young's modulus and Poisson's ratio, according to Eq. (6) - (11) and (13) - (14) evaluated for GV=GV_{avg} according to Eq. (15). The heterogeneous distribution of elastic properties across the tissue engineering scaffold is depicted in Fig. 3 and 4.

3.2 Evaluation of simulated uniaxial test: determination of longitudinal macroscopic Young's modulus

The FE models developed in the last subsection are subjected to uniaxial compression conditions in vertical (longitudinal) direction (orthogonal to the rapid-prototyped "beams", "piled" on each other), indicated by unit vector $\mathbf{e}_3$. Based on the Abaqus simulation package (Abaqus 6.10-2, Simulia, USA), a vertical displacement of magnitude $\Delta l_3 = 0.05 l_3$, l_3=5.46mm being the height of the scanned scaffold portion measured in $\mathbf{e}_3$ direction, is prescribed at the top surface of the scaffold. The bottom surface is held at fixed displacements in $\mathbf{e}_3$ direction, i.e. in the direction of the applied displacement, while this surface is free to deform in the plane orthogonal to $\mathbf{e}_3$. The lateral walls of the scaffold are kept stress-free. After stiffness matrix inversion and determination of internal forces, the resulting reaction force F (being the sum of all reaction forces in $\mathbf{e}_3$ direction triggered at the nodes of the upper surface of the finite element mesh) is used for evaluation of a macroscopic, whole scaffold-related, Young's modulus (E_{FE}) asfollows

$$E_{FE} = \frac{F l_3}{A \cdot \Delta l_3} \tag{16}$$

with A as the area of the loaded surface. The corresponding results are depicted in Fig. 5, as a function of the number of elements making up the respective FE meshes, resulting from the voxel merging procedure described in Section 3.1.

It becomes obvious that all meshes deliver, numerically speaking, fully converged results, i.e. the entity of all displacement shape functions of all elements satisfactorily represents the deformation of the investigated structure. Also, the overall deformation under macroscopic uniaxial load is fairly independent on the actual microscopic distribution of elastic properties, as can be seen from fair agreement of the results obtained from simulations based on heterogeneous and homogeneous material properties, respectively (see Tab. 2).

Still, we are left with the question whether the physical representation of the scaffold, i.e. the assignment of the (element-specific or overall averaged) elastic properties was reasonable. Therefore, we compare the macroscopic elastic modulus derived from the FE simulations with direct measurements of this property, as described next.

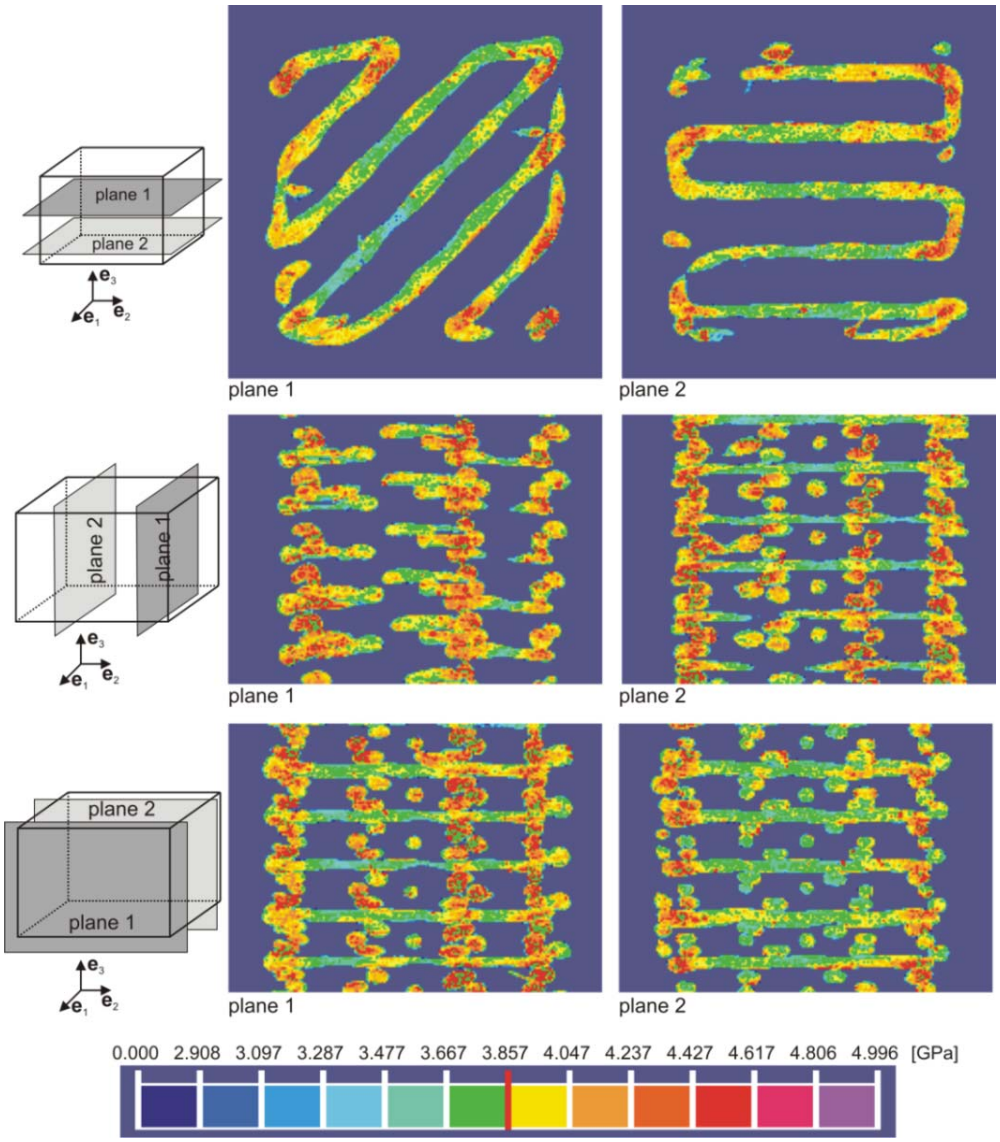

Figure 3: Young's modulus distribution in three orthogonal cross-sections of the heterogeneous FE model composed of 1.1×10^5 finite elements

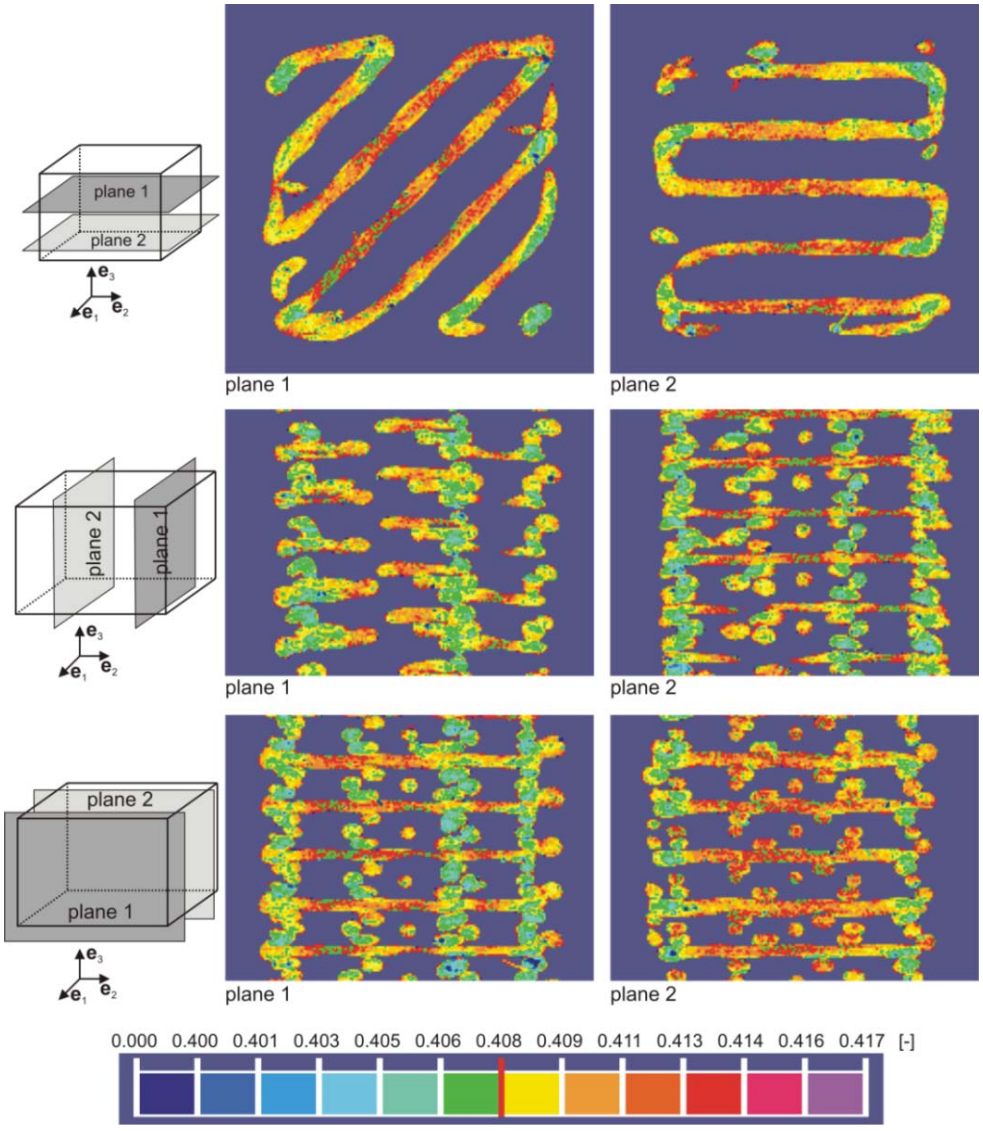

Figure 4: Poisson's ratio distribution in three orthogonal cross-sections of the heterogeneous FE model composed of 1.1×10^5 finite elements

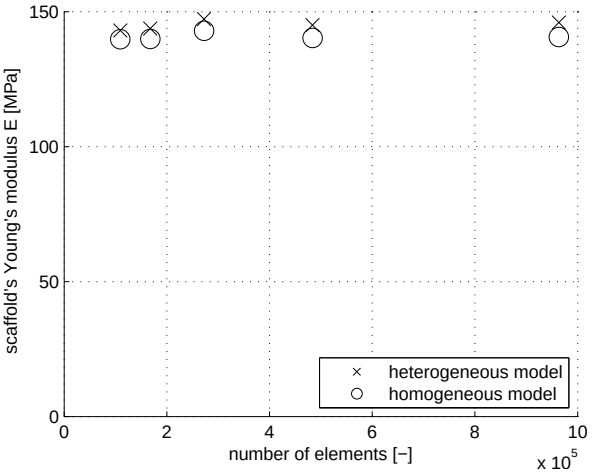

Figure 5: Young's modulus of the macroporous scaffold computed from homogeneous and heterogeneous FE simulations,based on meshes with different numbers of elements

Table 2: FE-predicted macroscopic scaffold-related Young's modulus averaged over the values given in Fig. 5, for homogeneous and heterogeneous microscopic elastic properties

	$< E_{FE} >$ [MPa]
heterogeneous model	145.02±1.68
homogenous model	140.71±1.28
averaged over both models	142.86±2.68

4 Experiments for model validation: quasi-static loading-unloading tests

Experimental determination of macroscopic elasticity is a delicate issue, since, e.g. due to not perfectly plane specimen surfaces, inelastic phenomena may occur right from the beginning of loading. As a remedy, we recall from thermodynamics [Salençon (2001)] that elasticity is related to the energy which can be released as efficient mechanical work, and this release is made possible through unloading of the sample (which is similar to what is done in standard nanoindentation protocols). Accordingly, the microCT-scanned tissue engineering scaffold sample was uniaxially tested in an electromechanical testing stand (LFM 150, Wille Geotechnik, Germany). Thereby, first a „slightly-above-zero" compressive load of approximately 5N was applied, in order to generate sufficient initial contact between the tested sample and the stamp.Then, the scaffold sample was repeatedly loaded and

unloaded, up to increasing compressive nominal strain levels, namely -0.02, -0.03, -0.04, and -0.05. Thereby, nominal strain (ε) is defined as:

$$\varepsilon = (h_3 - h_{3,0})/h_{3,0} \tag{17}$$

with h_3 and $h_{3,0}$ being the heights in the loading direction, of the deformed and the undeformed sample, respectively. During each cycle, both loading and unloading were performed with a displacement rate of 4mm/min, relating to a strain rate of 0.005s^{-1}. This is a typical quasi-static strain rate for biological and biomimetic materials [Brynk et al. (2011)]. Force-displacement curves were recorded throughout the whole procedure, and the unloading regimes of these curves were evaluated. From the load maxima at the aforementioned maximum strain levels and the corresponding displacements, the unloading curve was followed for a minimum of 50μm along the displacement axis, and a maximum of 350μm, in 50μm intervals. These different unloading portions were checked with respect to their linearity (indicating linear elastic properties as discussed throughout this article), in terms of R^2, the coefficient of determination between the measured forces and displacements. The slopes S of all unloading portions with $R^2 > 0.90$ are used to determine the Young's modulus of the macroporous scaffold according to

$$E_{unl} = Sh_3/A \tag{18}$$

with A as the cross sectional area perpendicular to the loading direction.

In this way, we obtain an experimental macroscopic Young's modulus of the scaffold of E_{unl}=125.5$\pm$19.33MPa(mean value $\pm$ standard deviation evaluated over 17 unloading branches).This value perfectly confirms the relevance of our simulated value of E_{FE}=142.86$\pm$2.68MPa (mean value $\pm$ standard deviation evaluated over all simulations recorded in Fig. 5, see also Tab. 2). This supports our confidence into the chosen modeling approach combining X-ray physics and analytical micromechanics with finite element technology, and to report in detail the simulation results obtained from our models.

5 Key results of Finite Element simulations

In addition to the macroscopic longitudinal Young's modulus of the scaffold, also the scaffold's transverse Poisson's ratios$\nu_{\mathbf{zx}}$ and $\nu_{\mathbf{zy}}$ can be determined from the FE simulations described above according to the following procedure: the displacements of points on each of the six mutually perpendicular or parallel surfaces of the roughly box-shaped scaffold were averaged over the respective surface. The resulting displacement components in the direction normal to the respective surface are denoted as u_i^+ and u_i^-, i=1,2,3, indicating the positive or negative surface

normal direction, and these components are defined as positive values when the respective points move in i-direction. Together with the scaffolds lineal dimension in i-direction, denoted as l_i, the aforementioned averaged displacement components give access to the macroscopic, whole scaffold-related normal strain components, in the form

$$E_{ii} = (u_i^+ - u_i^-)/l_i; \text{ for } i = 1,2,3 \tag{19}$$

These normal strains allow for determination of the Poisson's ratios measuring the lateral effects of longitudinal stress in the two transverse directions $\mathbf{e}_1$ and $\mathbf{e}_2$,

$$\nu_{31} = -E_{11}/E_{33} \quad \nu_{32} = -E_{22}/E_{33} \tag{20}$$

The resulting macroscopic Poisson's ratios are reported in Fig. 6 and Tab. 3. As it was the case with the longitudinal macroscopic Young's modulus, they do not vary too much between the simulations based on heterogeneous material properties, and those based on homogeneous properties. Also, the rather small difference between ν_{32} and ν_{31} suggests that, in a first approximation, the scaffold, at the macrosale, might be regarded as roughly cubic, hencea quasi-cubic Poisson's ratio averaged over all values depicted in Fig. 6, amounts to 0.0638 ± 0.0136.

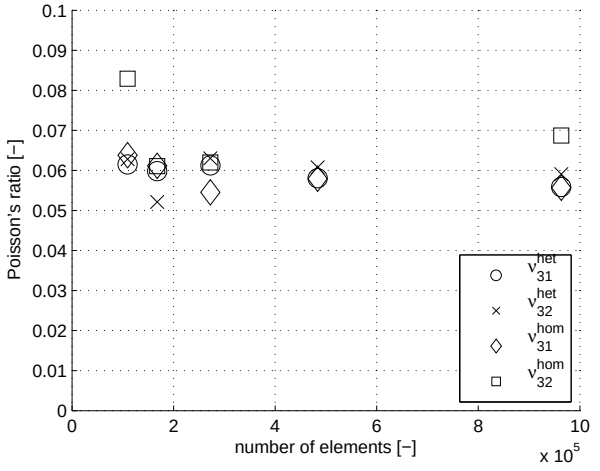

Figure 6: Transverse Poisson's ratios of the macroscopic scaffold computed from homogeneous and heterogeneous FE simulations,based on meshes with different numbers of elements

It is remarkable that the macroscopic Poisson's ratio is significantly lower than that of the PLLA-TCP composite solid (amounting to 0.44, see Tab.1). This indicates

Table 3: Transverse Poisson's ratios of the macroscopic scaffold computed from FE simulations, based on a mesh with 1.1×10^5 number of elements

	ν_{31} [-]	ν_{32} [-]
heterogeneous model	0.0593±0.0024	0.0596±0.0045
homogenous model	0.0586±0.0038	0.0779±0.0224
averaged over both models	0.0590±0.0030	0.0687±0.0180

that, on the microstructural level, the solid phase undergoes much less deformations and strains than the pore phase. In order to quantify this effect, we apply the strain average rule of micromechanics [Zaoui (2002)] to the entire scaffold, which allows us to derive from the average microstrain components in the solid phase ε^s_{ij}, i, j=1,2,3, obtained directly from the simulations, the average strains ε^p_{ij}, i, j=1,2,3 in the pores, according to

$$\varepsilon^p_{ij} = [E_{ij} - (1-\Phi)\varepsilon^s_{ij}]/\Phi; \text{ or } i, j = 1,2,3 \tag{21}$$

with Φ as the macroporosity of the scaffold, as determined in Section 2.1. Indeed, the average vertical normal strains in the pores are much larger than those in the solid (compare ε_{33} and ε_{33} in Tab. 4 and 5). This is consistent with the very localized ("concentrated") stress and strain peaks in the solid, occurring *only* at the joints between the individual "struts" "piled" one above the other, see Fig. 7 and 8 for principal stress and strain distributions across the investigated structure. The shear microstrains, both in the solid and in the pores, are at least two orders of magnitude smaller than the normal microstrains, which indicates that the overall scaffold's deformation process is largely "free" from shear deformations.

Table 4: Microstrains averaged over solid compartment of scaffold$<\varepsilon^s>$, for heterogeneous and homogeneous simulations with 1.1×10^5 elements; index "3" labels (longitudinal) loading direction, indices "1" and "2" label (transverse) orthogonal to the loading directions

	$<\varepsilon^s_{11}>$ [-]	$<\varepsilon^s_{22}>$ [-]	$<\varepsilon^s_{33}>$ [-]
heterogeneous model	$(0.24 \pm 0.00)\times10^{-2}$	$(0.24 \pm 0.00)\times10^{-2}$	$(-0.54 \pm 0.02)\times10^{-2}$
homogenous model	$(0.24 \pm 0.00)\times10^{-2}$	$(0.24 \pm 0.00)\times10^{-2}$	$(-0.54 \pm 0.02)\times10^{-2}$

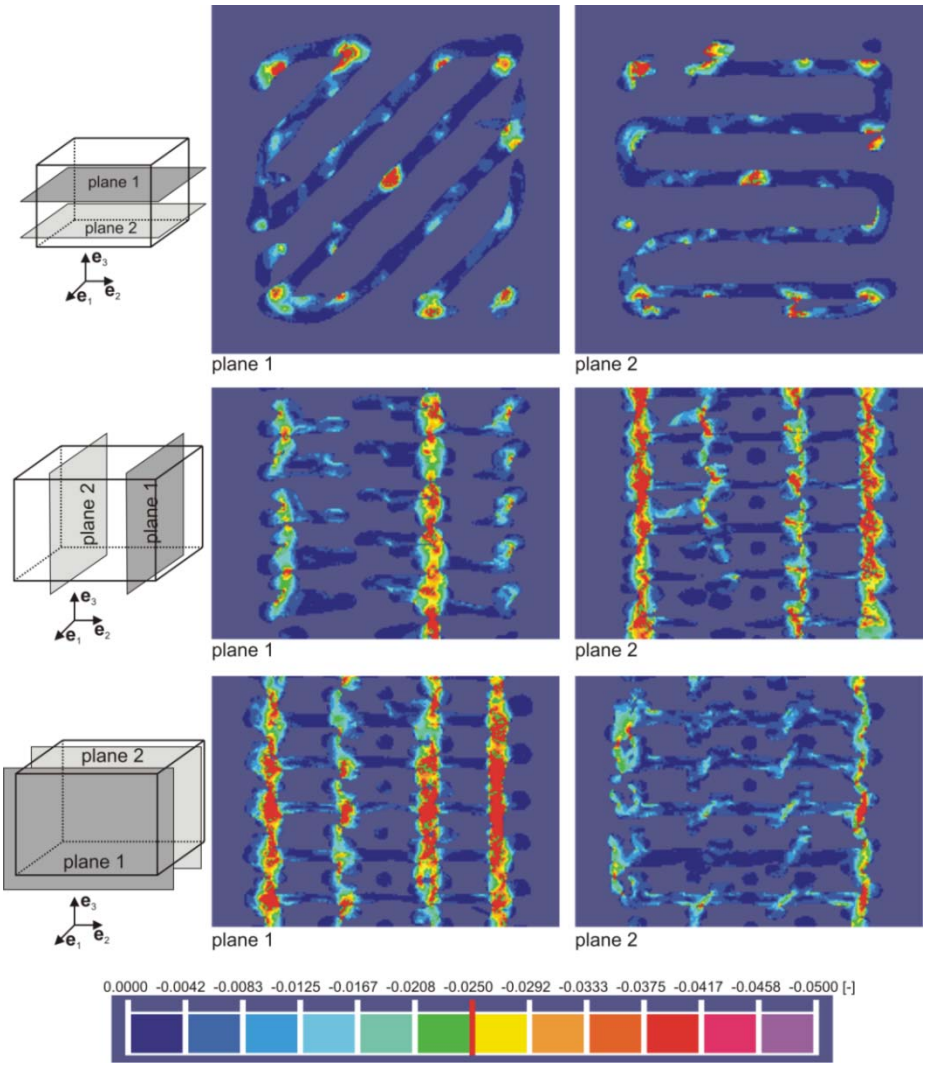

Figure 7: Minimum principal strain distribution in three orthogonal cross-sections through the scaffold, derived from the heterogeneous simulation based on a mesh with 1.1×10^5 elements

Table 5: Average microstrains in pores $<\varepsilon^s>$, computed from average microstrains in solid and macro strains according to Eq. (21), for heterogeneous and homogeneous simulations with 1.1×10^5 elements; index "3" labels (longitudinal) loading direction, indices "1" and "2" label (transverse) orthogonal to the loading directions

	$<\varepsilon^p_{11}>$ [-]	$<\varepsilon^p_{22}>$ [-]	$<\varepsilon^p_{33}>$ [-]
heterogeneous model	0.32×10^{-2}	0.32×10^{-2}	-6.83×10^{-2}
homogenous model	0.31×10^{-2}	0.45×10^{-2}	-6.83×10^{-2}

Next, we wish to discuss the effect of considering heterogeneous versus homogeneous elastic properties across the solid part of the investigated scaffold. Therefore, it is beneficial [Dejaco et al. (2012)] to compute first-order as well as second-order moments of deviatoric stresses, averaged over the solid portion of the scanned scaffold, forming the Finite Element mesh. In mathematical terms, the deviatoric stress tensor reads as

$$\boldsymbol{\sigma}_{dev}(\mathbf{x}) = \boldsymbol{\sigma}(\mathbf{x}) - \frac{1}{3}\mathbf{1}tr(\boldsymbol{\sigma}(\mathbf{x})) \tag{22}$$

where $\boldsymbol{\sigma}$ is the Cauchy stress tensor, $\mathbf{x}$ gives the position of the considered finite element, *tr* is the trace operator, and $\mathbf{1}$ is the second-order unity tensor.

The first-order average of deviatoric stresses is evaluated according to [Dormieux et al. (2002)]

$$\overline{\sigma}_{dev} = \sqrt{\frac{1}{2}\langle\boldsymbol{\sigma}_{dev}(\mathbf{x})\rangle : \langle\boldsymbol{\sigma}_{dev}(\mathbf{x})\rangle} \tag{23}$$

with

$$\langle(\cdot)\rangle = \frac{1}{V_s}\int_{V_s}(\cdot)\,dV \tag{24}$$

as the average of quantity $(\cdot)$ over all (solid) finite elements, filling volume V_s. The second-order average of deviatoric stresses is evaluated as [Dormieux et al. (2002)]

$$\overline{\overline{\sigma}}_{dev} = \sqrt{\frac{1}{2}\langle\boldsymbol{\sigma}_{dev}(\mathbf{x}) : \boldsymbol{\sigma}_{dev}(\mathbf{x})\rangle} \tag{25}$$

As a result, the homogeneous model delivered a marginally lower value of the first order moment of deviatoric stresses than the heterogeneous one (see Tab. 6). This means that the homogeneous model is slightly softer than the heterogeneous one, which is in agreement with the macroscopic Young's moduli reported in Tab. 1.

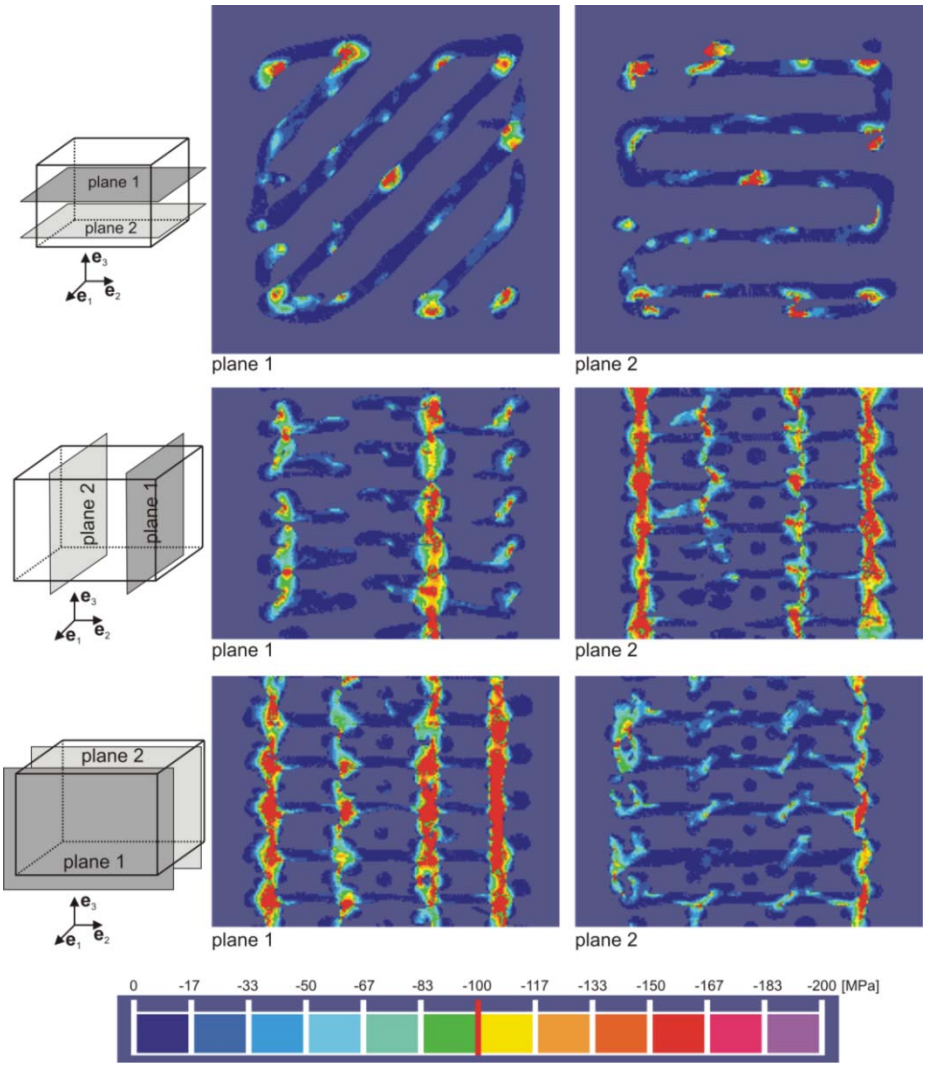

Figure 8: Minimum principal stress distribution in three orthogonal cross-sections through the scaffold, derived from the heterogeneous simulation based on a mesh with 1.1×10^5 elements

Also the second order moment of deviatoric stresses was (albeit only slightly) higher in the heterogeneous model than in the homogeneous one (see Tab. 6). This indicates a slightly higher heterogeneity of the microstress distribution in the heterogeneous as compared to the homogeneous simulations.

Table 6: First and second order moments of deviatoric stresses computed for heterogeneous an homogeneous FE models with 1.1×10^5 elements

deviatoric stresses [MPa]	heterogeneous model	homogenous model
first-order moment	15.16	14.81
second-order moment	43.57	42.43

6 Conclusion

Young's modulus of a macroporous tissue engineering scaffold made of PLLA with TCP inclusions can be well estimated from FE models based on merging of microCT voxels into finite elements of regular meshes, and relating the X-ray attenuation values, via the rules of X-ray physics and micromechanics, into finite element-specific elastic properties. Both heterogeneous and homogeneous models deliver results which agree well with experimental values of quasi-static uniaxial unloading tests. This indicates the significant homogeneity of the produced scaffold. Close investigation of simulation results, such as microstresses and microstrains both in the solid and in the pores, show that the strains in the solid phase are concentrated at the junctions between the rapid-prototyped "beams", so that the average pore microstrains are much larger than the average solid microstrains, which is also expressed by macroscopic Poisson's ratios being much smaller than the Poisson's ratio of the solid (nano)composite made up by PLLA and TCP.

Acknowledgement: The experimental campaign as well as the basis for the grey values translation strategy was developed, between December 2009 and November 2011, as part of the project BIO-CT-EXPLOIT (grant number 232164), in the framework of the Seventh Framework Program of the European Commission (FP7), theme FP7-2008-SME-1. Completion of the attenuation-to-elasticity conversion and of the series of Finite Element simulations after November 2011, as well as detailed evaluation of the results became possible through the project MICROBONE (grant number 257023), granted by the European Research Council (ERC). The authors gratefully acknowledge the support of Roland Reihsner during the performance of the quasi-static tests.

References

Balac, I.; Uskokovic, P.S.; Aleksic, R.; Uskokovic, D. (2002): Predictive Modeling of the Mechanical Properties of Particulate Hydroxyapatite Reinforced Polymer Composites. *Journal of Biomedical Materials Research*, vol. 63, no. 6, pp. 793-799.

Benveniste, Y.A. (1987): A new approach to the application of Mori-Tanakas theory in composite materials. *Mechanics of Materials*, vol. 6, pp. 147-157.

Bertrand, E.; Hellmich, C. (2009): Multiscale Elasticity of Tissue Engineering Scaffolds with Tissue-Engineered Bone: A Continuum Micromechanics Approach. *Journal of Engineering Mechanics (ASCE)*, vol. 135, no. 5, pp. 395-412.

Blazewicz, S.; Stoch, L. (2004): *Biocybernetyka i i?ynieria Biomedyczna2000. Tom 4 Biomaterialy*[*Biocybernetics and Biomedical Engineering 2000. Part 4 Biomaterials]*. Akademicka oficyna Wydawnicza EXIT, Warszawa, Poland (in Polish).

Brynk, T.; Hellmich, C.; Fritsch, A.; Zysset, P.; Eberhardsteiner, J. *(2011):Experimental poromechanics of trabecular bone strength: role of Terzaghi's effective stress and of tissue level stress fluctuations. Journal of Biomechanics, vol. 44, no. 3, pp. 501-508.*

Chen, Y.; Feng, B.; Zhu, Y.; Weng, J.; Wang, J.; Lu, X. (2011): Preparation and characterization of a novel porous titanium scaffold with 3D hierarchical porous structures. *Journal of Materials Science*, vol. 22, pp. 839-844.

Crawley, E.O.; Evans, W.D.; Owen, G.M. (1988): A theoretical analysis of the accuracy of single-energy CT bone-mineral measurements. *Physics in Medicine and Biology*, vol. 33, no. 10, pp. 1113-1127.

Dejaco, A.; Komlev, V.S.; Jaroszewicz, J.; Swieszkowski, W.; Hellmich, C. (2012): Micro CT-based multiscale elasticity of double-porous (pre-cracked) hydroxyapatite granules for regenerative medicine. *Journal of Biomechanics* vol 45, pp. 1068-1075.

Dormieux, L.; Kondo, D.; Ulm, F.J. (2006):Microporomechanics. Wiley.

Dormieux, L.; Molinari, A.; Kondo, D. (2002): Micromechanical approach to the behavior of poroelastic materials. *Journal of the Mechanics and Physics of Solids*vol. 50, no. 10, pp. 2203–2231.

Dorozhkin, S.V. (2009): Calcium orthophosphates in nature, biology, and medicine. *Materials* vol. 2, pp. 399-498.

Eshelby, J.D. (1957): The determination of the elastic field of an ellipsoidal inclusion, and related problems. *Proceedings of the Royal Society of London. Series A, Mathematical and Physical Sciences*, vol. 241, pp. 376-396.

Fritsch, A.; Dormieux, L.; Hellmich, C.; Sanahuja, J. (2009): Mechanical behavior of hydroxyapatite biomaterials: An experimentally validated micromechanical model for elasticity and strength.*Journal of Biomedical Materials Research Part A*, vol. 88A, pp. 149-161.

Garlotta, D. (2001): A Literature Review of Poly(Lactic Acid). *Journal of Polymers and Environment* vol. 9, no. 2, pp. 63-84.

Hellmich, C.; Kober, C.; Erdmann, B. (2008): Micromechanics-Based Conversion of CT Data into Anisotropic Elasticity Tensors, Applied to FE Simulations of a Mandible. *Annals of Biomedical Engineering*, vol. 36, no. 1, pp. 108–122.

Janicki, P.; Schmidmaier, G. (2011): What should be the characteristics of the ideal bone graft substitute? Combining scaffolds with growth factors and/or stem cells. *Injury*, vol. 42, no. 2, pp. 77-81.

Katz, J.L.; Ukraincik, K. (1971): On the anisotropic elastic properties of hydroxyapatite. *Journal of Biomechanics* vol. 4, pp. 221-227.

Khademhosseini, A.; Langer, R.; Borenstein, J.; Vacanti, J.P. (2005): Microscale technologies for tissue engineering and biology. *Proceedings of the National Academy of Sciences of the United States of America* vol. 103, no. 8, pp. 2480-2487.

Khanna, R.; Katti, K.S.; Katti, D.R. (2009): Nanomechanics of Surface Modified Nanohydroxyapatite Particulates Used in Biomaterials. *Journal of Engineering Mechanics*, vol. 135, no. 5, pp. 468-478

Komlev, V.S.; Mastrogiacomo, M.; Pereira, R.C.; Peyrin, F.; Rustichelli, F.; Cancedda, R. (2010): Biodegradation of porous calcium phosphate scaffolds in an ectopic bone formation model studied by X-ray computed microtomography. *European Cells and Materials*, vol. 19, pp. 136-146.

Lacroix, D.; Chateau, A.; Ginebra, M.; Planell, J.A. (2006): Micro-finite element models of bone tissue-engineering scaffolds. *Biomaterials* vol. 27, pp. 5326–5334.

Langer, R.; Vacanti, J.P. (1993): Tissue engineering. *Science*, vol. 260, no. 5110, pp. 920-926.

Luczynski, K.; Brynk, T.; Ostrowska, B.; Swieszkowski, W.; Reihsner, R.; Hellmich, C.(2012): Consistent quasi-static and acoustic elasticity determination of PLLA-based rapid-prototyped tissue engineering scaffolds. Journal of Biomedical Materials Research Part A,DOI: 10.1002/jbm.a.34316, available online at `http://onlinelibrary.wiley.com/`.

Mori, T.; Tanaka, K. (1973): Average stress in matrix and average elastic energy of materials with misfitting inclusions. *Acta Metallurgica* vol. 21, no. 5, pp. 571-

574.

Mouriño, V.; Cattalini, J.P.; Boccaccini, A.R. (2012): Metallic ions as therapeutic agents in tissue engineering scaffolds: An overview of their biological applications and strategies for new developments. *Journal of the Royal Society Interface* vol. 9, no. 68, pp. 401-419.

Oliver, W.C.; Pharr, G.M. (2004): Measurement of hardness and elastic modulus by instrumented indentation: Advances in understanding and refinements to methodology. *Journal of Materials Research* vol. 19, no. 1, pp. 3-20.

Park, H.; Cannizzaro, C.; Vunjak-Novakovic, G.; Langer, R.; Vacanti, C.A.; Farokhzad, O.C. (2007): Nanofabrication and microfabrication of functional materials for tissue engineering. *Tissue Engineering* vol 13, no. 8, pp. 1867-1877.

Popper K.R. (1934): *Logik der Forschung*[*The logic of scientific discovery*]. Springer, Vienna, Austria (in German).

Rezwan, K.; Chen, Q.Z.; Blaker, J.J.; Boccaccini, A.R. (2006): Biodegradable and bioactive porous polymer/inorganic composite scaffolds for bone tissue engineering. *Biomaterials*, vol. 27, pp. 3413-3431.

Salençon, J. (2001): *Handbook of Continuum Mechanics*. Springer.

Sandino, C.; Planell, J.A.; Lacroix, D. (2008): A finite element study of mechanical stimuli in scaffolds for bone tissue engineering. *Journal of Biomechanics*, vol. 41, no. 5, pp. 1005-1014.

Scheiner, S.; Sinibaldi, R.; Pichler, B.; Komlev, V.; Renghini, C.; Vitale-Brovarone, C.; Rustichelli, F.; Hellmich, C. (2009): Micromechanics of Bone Tissue-Engineering Scaffolds, Based on Resolution Error-Cleared Computer Tomography. *Biomaterials*, vol. 30, pp. 2411-2419.

Swieszkowski, W.; Tuan, B.H.; Kurzydlowski, K.J.; Hutmacher, D.W. (2007): Repair and regeneration of osteochondral defects in the articulat joints. *Biomolecular Engineering*,vol. 24, no. 5, pp. 489-495.

Wagoner Johnson, A.J.; Herschler, B.A. (2011): A review of the mechanical behavior of CaP and CaP/polymer composites for applications in bone replacement and repair. *Acta Biomaterialia*, vol. 7, pp. 16-30.

Woodard, J.R.; Hilldore, A.J.; Lan, S.K.; Park, C.J.; Morgan, A.W.; Eurell, J.A.; Clark, S.G.; Wheeler, M.B.; Jamison, R.D.; Wagoner Johnson, A.J. (2007): The mechanical properties and osteoconductivity of hydroxyapatite bone scaffolds with multi-scale porosity. *Biomaterials*, vol. 28, pp. 45-54.

Zaoui, A. (2002): Contnuum micromechanics: survey. *Journal of Engineering Mechanics (ASCE)*, vol. 128, no. 8, pp. 808-816.

Zienkiewicz, O. C.; Taylor, R. L. (2005): *The Finite Element Method Set*. Butter-

worth-Heinemann.